Journal of
Materials Chemistry B

PAPER

View Article Online
View Journal

Cite this: DOI: 10.1039/d5tb01135c

Construction of a sandwich-type DNA biosensor based on functionalized MOF@COF nanomaterials for the detection of NSCLC biomarker ctDNA†

Lin Fu,[a] Yan Zhang,[a] Peng Tang,[b] Huiling Chen,[a] Junxin Li,[a] Min Shi,[a] Yanyu Li,[a] Gongli Hu,[a] Zhongshu Wang,[a] Xiaolin Yu*[c] and Yi Xiao*[a]

Received 12th May 2025,
Accepted 19th July 2025

DOI: 10.1039/d5tb01135c

rsc.li/materials-b

As a key diagnostic biomarker for non-small cell lung cancer (NSCLC), the sensitive detection of circulating tumor DNA (ctDNA) is crucial for early-stage disease detection and monitoring. However, the existing detection methods still have limitations in terms of sensitivity, cost and operational simplicity. In this study, we successfully constructed a novel sandwich-structured electrochemical biosensor based on a methylene blue (MB)-based signal indication system, leveraging the synergistic effects of metal–organic frameworks (MOFs) and covalent organic frameworks (COFs), to realize the efficient quantitative analysis of ctDNA. The key innovation of this biosensor lies in the utilization of MOF@COF core–shell nanocomposites as signal amplifiers, combined with surface functionalization *via* gold nanoparticles (AuNPs) to form a MOF@COF@AuNPs double-layer core–shell nanocomposite. Firstly, through synthesizing the $\mathrm{COF_{TAPB\text{-}DMTP}}$ shell on the surface of the UiO-66-NH_2 MOF core, additional mesoporous diffusion channels were introduced between the MOF crystals, which can further increase the electron transfer rate of the electroactive substance MB. Secondly, the modification of AuNPs not only accelerates the electron transfer rate of the MOF@COF at the glassy carbon electrode (GCE) but also immobilizes large amounts of signal probes (SPs) and electroactive substances through the gold–nitrogen (Au–N) bond. The experimental results showed that the sensor exhibited a wide linear range from 1 fM to 100 nM, and the detection limit was as low as 0.31 fM. The results of clinical samples demonstrated that the method was effective in differentiating ctDNA levels between NSCLC patients and healthy populations. The electrochemical biosensor constructed using this strategy provides a potential analytical tool for early-stage clinical diagnosis of NSCLC.

1. Introduction

According to global cancer statistics for 2022, lung cancer remains the leading cause of cancer-related mortality worldwide, with approximately 2.5 million new cases and 1.8 million deaths annually.[1] Lung cancer is classified into non-small cell lung cancer (NSCLC) and small cell lung cancer (SCLC). The former accounts for 80% of all cases[2] and is usually diagnosed at an advanced stage, often too late for surgical intervention, resulting in very low survival rates.[3] Therefore, early-stage detection and diagnosis of NSCLC are important to improve its treatment outcomes. In recent years, the rapid development of clinical laboratory medicine and advances in research have highlighted the scientific significance and practical value of identifying serological biomarkers for the early diagnosis, efficacy monitoring, and prognosis assessment of cancer.[4,5]

Circulating tumor DNA (ctDNA), a type of extra-cellular DNA derived from the somatic DNA of tumor cells that is released into the circulatory system in a cell-free state after cell detachment or apoptosis, has been shown to have potential as a biomarker for early cancer detection and localization.[6–8] Compared with protein-based markers, ctDNA derived from genomic mutations in tumor cells has higher specificity.[9] Therefore, ctDNA detection provides a new direction for the early diagnosis of NSCLC. Currently, clinical methods for quantitative ctDNA analysis include the polymerase chain reaction (PCR)[10] and second-generation sequencing (NGS).[11] However, both methods have certain drawbacks, such as the need for high-precision instruments, cumbersome procedures, and high testing costs. Therefore, the development of low-cost, real-time, portable and easy-to-use ctDNA detection devices is essential for the screening and diagnosis of NSCLC.

---

[a] Department of Pharmacy, Zigong Fourth People's Hospital, Zigong, Sichuan 643000, P. R. China. E-mail: zgsyy450577@163.com

[b] School of Chemical Engineering, Sichuan University of Science and Engineering, Zigong, Sichuan 643000, P. R. China

[c] Department of Laboratory Medicine, Sichuan Clinical Research Center for Clinical Laboratory, Zigong Fourth People's Hospital, Zigong, Sichuan 643000, P. R. China. E-mail: yuxiaolincq@hotmail.com

† Electronic supplementary information (ESI) available. See DOI: https://doi.org/10.1039/d5tb01135c

Compared to conventional clinical ctDNA quantification methods, electrochemical DNA biosensors provide faster response times, higher sensitivity, and lower cost, enabling wide applicability in cancer biomarker detection.[12,13] DNA molecules exhibit excellent molecular recognition properties and can be easily modified to achieve high stability, making them attractive for biosensor design.[14,15] In order to convert DNA hybridization or aptamer binding events into detectable physical signals for trace analysis in practical applications, various nanomaterials have been widely utilized.[16–18]

Covalent organic frameworks (COFs) are porous crystalline organic polymers composed of elements such as C, H, O, N and B.[19] These materials are constructed through reversible covalent bonds, offering advantages such as high porosity, a large specific surface area, and low density.[20] However, pure COF materials often exhibit inherent weaknesses such as poor electrical conductivity and a lack of functional diversity.[21] Therefore, the development of COF-based hybrid materials is of strategic importance for achieving specific goals and desired properties. Currently, metal–organic frameworks (MOFs) and COF hybrid materials have attracted significant attention in the field of nanomaterials due to their complementary advantages such as high specific surface area, customizable structures and properties, and suitable band gaps.[22–25] Recently, Yu *et al.* developed lattice-reciprocal MOF@COF heterostructures exhibiting dynamic adaptive behavior, which exhibited excellent selectivity for formic acid and high CO_2 photoreduction yields.[26] Subsequently, Li *et al.* synthesized hierarchical porous MOF@COF core–shell structures to achieve efficient separation of C_2H_6/C_2H_4.[27] These studies demonstrate that well-designed MOF@COF composite systems with core–shell structures show great potential for multiphase catalytic applications. However, the functionalization of sensors with core–shell MOF@COF materials for quantitative biomarker detection has not yet been thoroughly explored.

This study developed an electrochemical biosensor for ultrasensitive detection of an NSCLC ctDNA biomarker. Specifically, the polyethyleneimine (PEI) functionalized nitrogen-doped graphene (P-NG) composite modified with gold nanoparticles (P-NG-AuNPs) was immobilized on the electrode surface. This step aimed to enhance the dispersion of the composite and specific surface area of the GCE, which in turn increased the number of binding sites for the capture probe (CP) and laid the foundation for stable electrochemical signal output. Next, a novel MOF@COF nanomaterial was synthesized and employed as a carrier for the electroactive substance methylene blue (MB) to amplify the electrochemical signals by utilizing its porous structure and strong adsorption capacity. After modification with AuNPs, MOF@COF@MB@AuNPs were labeled with the signal probe (SP) to ultimately form the signaling tracer MOF@COF@MB@AuNPs-SP (tracer label). When the target analyte ctDNA is present, one end binds to the CP immobilized on the electrode surface, while the other end binds to the SP. This process brought MB to the electrode surface, forming a stable sandwich-type biosensor. Finally, the current response of MB was recorded by differential pulse voltammetry (DPV), thus achieving highly sensitive detection of ctDNA.

2. Experimental

Details regarding the reagent materials and equipment used in this experiment are provided in Sections S1 and S2 (ESI†).

2.1. Preparation of the P-NG-AuNP composite

AuNPs were synthesized based on previously reported literature,[28] as described in detail in Section S3 (ESI†). Next, 4 mg of NG was added to 4 mL of DMF solution in a beaker and the mixture was stirred for 24 h. Afterward, the mixture was washed twice with deionized water and replenished with 4 mL of fresh deionized water in the same beaker. Next, 2 mL of AuNP dispersion was added to the system. The mixture was stirred for 8 h, thoroughly rinsed with deionized water, and dried to yield the P-NG-AuNP composite, which was stored at 4 °C.

2.2. Preparation of UiO-66-NH_2

UiO-66-NH_2 was synthesized according to the hydrothermal method reported by Zhang *et al.* with slight modifications.[29] After H_2BDC (83 mg, 0.5 mmol) and $ZrCl_4$ (116 mg, 0.5 mmol) were completely dissolved in 20 mL of DMF, 4 mL of formic acid (FA) was added followed by 20 min of stirring at room temperature. The solution was then transferred to a 50 mL Teflon-lined autoclave and heated to 120 °C for 24 h. After cooling to room temperature, the product was washed sequentially with methanol and DMF *via* centrifugation. Finally, the wet sample was dried at 80 °C to obtain a white UiO-66 powder.

The dried UiO-66 powder (60 mg) and H_2BDC-NH_2 (36 mg) were dispersed in 20 mL of DMF. The mixture was stirred for 20 min to ensure complete dissolution of H_2BDC-NH_2, then transferred to a 50 mL Teflon-lined autoclave and heated to 120 °C for 24 h. Upon cooling to room temperature, the product was sequentially washed with DMF and methanol *via* centrifugation and dried at 80 °C.

2.3. Preparation of UiO-66-NH_2@$COF_{TAPB\text{-}DMTP}$

Based on the previously reported literature,[27] we used the covalent linkage method to prepare UiO-66-NH_2@$COF_{TAPB\text{-}DMTP}$. Firstly, 20 mg of UiO-66-NH_2 was placed in a 10 mL centrifuge tube and subsequently dispersed homogeneously in 4 mL of acetonitrile solution using the sonication technique. Next, 7.5 mg of DMTP was added to this dispersion system, and this step was immediately followed by the addition of 0.2 mL of HAc. Subsequently, the test tube was shaken vigorously for approximately 20 seconds to ensure thorough mixing. The mixture was then allowed to stand at room temperature for 12 h. Next, 1 mL of acetonitrile (ACN) solution containing 8.8 mg of TAPB and 0.2 mL of HAc was added to the mixture. The tube was shaken vigorously again for 20 seconds to achieve homogeneous mixing and was allowed to continue standing at room temperature for 3 days. Finally, the resulting yellow precipitate was collected by centrifugation, washed several times with ethanol, and dried at 80 °C for 4 h.

2.4. Preparation of the tracer label

Firstly, 500 μL of AuNPs was added to the UiO-66-NH_2@$COF_{TAPB\text{-}DMTP}$ (1 mg mL^{-1}) solution and stirred for 6 h; after centrifugation (8000 rpm, 5 min), the composite solution was obtained. Subsequently, 1 mL of 0.2 mg mL^{-1} MB solution was added to the composite solution and the mixture was stirred continuously for 24 h. The solution was washed with deionized water to obtain UiO-66-NH_2@$COF_{TAPB-DMTP}$@MB@AuNPs, and finally 200 μL of SP was added to the solution under ice-bath conditions and stirred overnight. After centrifugation and washing, 1 mL of deionized water was added to obtain the tracer label (UiO-66-NH_2@$COF_{TAPB-DMTP}$@MB@AuNPs-SP), which was then stored at 4 °C for further use.

2.5. Assembly process of the electrochemical biosensor

Firstly, the glassy carbon electrode (GCE) needs to be pretreated before proceeding with the construction of the biosensor, as detailed in Section S4 (ESI†). Subsequently, 10 μL of a 1 mg mL^{-1} suspension of P-NG-AuNPs was drop-cast onto the GCE and dried. Next, 10 μL of the CP (2 μM) was incubated on the surface of the P-NG-AuNPs/GCE for 6 h to form the CP/P-NG-AuNPs/GCE. To inhibit the non-specific binding of ctDNA, the resulting CP/P-NG-AuNPs/GCE was incubated with 10 μL of 1.0 wt% BSA for 30 min.

2.6. Electrochemical determination of ctDNA

Firstly, 10 μL of ctDNA solutions with varying concentrations was dropwise added to the CP/P-NG-AuNPs/GCE surface. To ensure sufficient interaction between the solution and the electrode, the system was incubated at 4 °C for 3 h. Subsequently, 10 μL of tracer label solution was carefully added to the modified electrode and further incubated at 4 °C for 1.5 h. During this process, when the target analyte ctDNA was present, the signaling probe (SP) hybridized specifically with ctDNA through complementary base pairing, thereby introducing the tracer label onto the electrode surface. Finally, electrochemical signals were recorded by differential pulse voltammetry (DPV) in phosphate buffer solution (PBS, pH 7.0) with the scan potential ranging from −0.6 V to 0.1 V to ensure data accuracy (Scheme 1).

3. Results and discussion

3.1. Characteristics of different composites

The morphology and size of the P-NG-AuNPs nanocomposite were characterized by scanning electron microscopy (SEM). As shown in Fig. 1A, NG exhibited an obvious fold-like morphology, indicating a high specific surface area.[30] AuNPs were uniformly dispersed on the NG surface (Fig. 1B), confirming the successful synthesis of P-NG-AuNPs.

The SEM image (Fig. 1C) showed that the pristine UiO-66-NH_2 exhibited a regular octahedral morphology with a smooth surface.[31] After coating with $COF_{TAPB-DMTP}$, the UiO-66-NH_2@$COF_{TAPB-DMTP}$ composite retained a similar octahedral morphology, while its surface displayed pronounced roughness

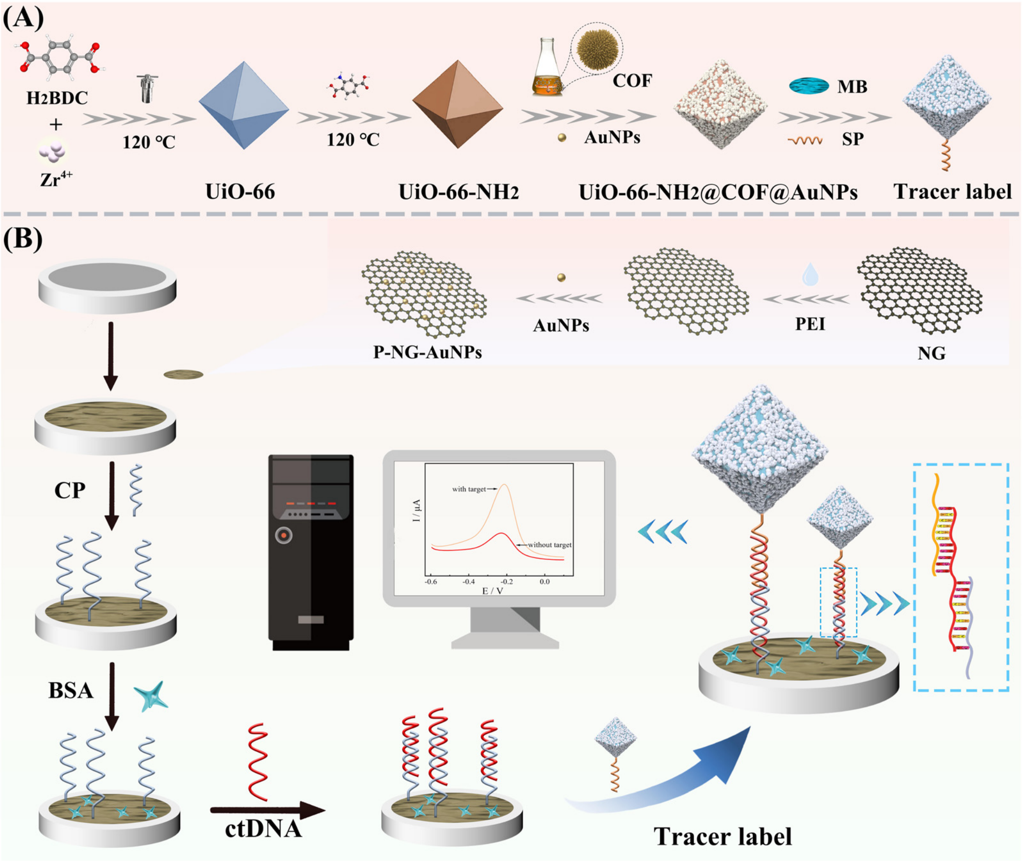

Scheme 1 Schematic illustration of the electrochemical biosensor for ctDNA.

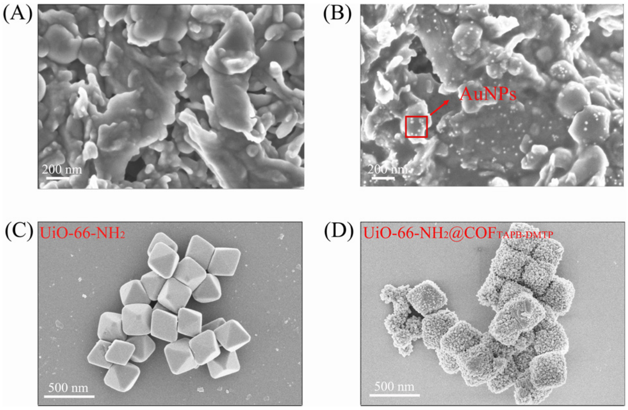

Fig. 1 SEM images of (A) NG, (B) P-NG-AuNPs, (C) UiO-66-NH_2 and (D) UiO-66-NH_2@$COF_{TAPB-DMTP}$.

(Fig. 1D). These results demonstrate the successful synthesis of a core–shell MOF@COF nanomaterial. The COF shell enhances the electron transfer rate of methylene blue (MB) by introducing mesoporous diffusion channels between MOF crystals.[27]

The novel core–shell material UiO-66-NH_2@$COF_{TAPB-DMTP}$ was further characterized by transmission electron microscopy (TEM), X-ray diffraction (XRD) and Fourier transform infrared spectroscopy (FT-IR).

The core–shell structure of the MOF@COF was systematically characterized by TEM. As shown in Fig. 2A, the aldehyde structural units of $COF_{TAPB-DMTP}$ were uniformly anchored on the MOF surface, consistent with SEM observations and indicative of a regular crystal structure. Further experimental results incorporating noble metal nanoparticle modification showed that after *in situ* loading by AuNPs, metal nanoparticles with an average particle size of about 20 nm were uniformly distributed on the surface of the material (Fig. S1, ESI†). Elemental surface scanning analysis showed that the substrate elements, such as C, N, O, and Zr, were uniformly co-distributed with Au elements in three-dimensional space (Fig. 2C). As shown in Fig. 2D, energy dispersive X-ray spectroscopy (EDS) further confirmed the existence of the above elements.

Moreover, compared to the FT-IR spectrum (Fig. 2E) of pristine UiO-66-NH_2, a new characteristic peak was observed at 1620 cm^{-1} (C=N) in the spectrum of UiO-66-NH_2@$COF_{TAPB-DMTP}$, confirming the formation of a Schiff base and the successful growth of the $COF_{TAPB-DMTP}$ shell on the UiO-66-NH_2. The XRD patterns (Fig. 2F) of the UiO-66-NH_2@$COF_{TAPB-DMTP}$ show a characteristic peak at 2.5° at 2θ degree. After modification by AuNPs, it

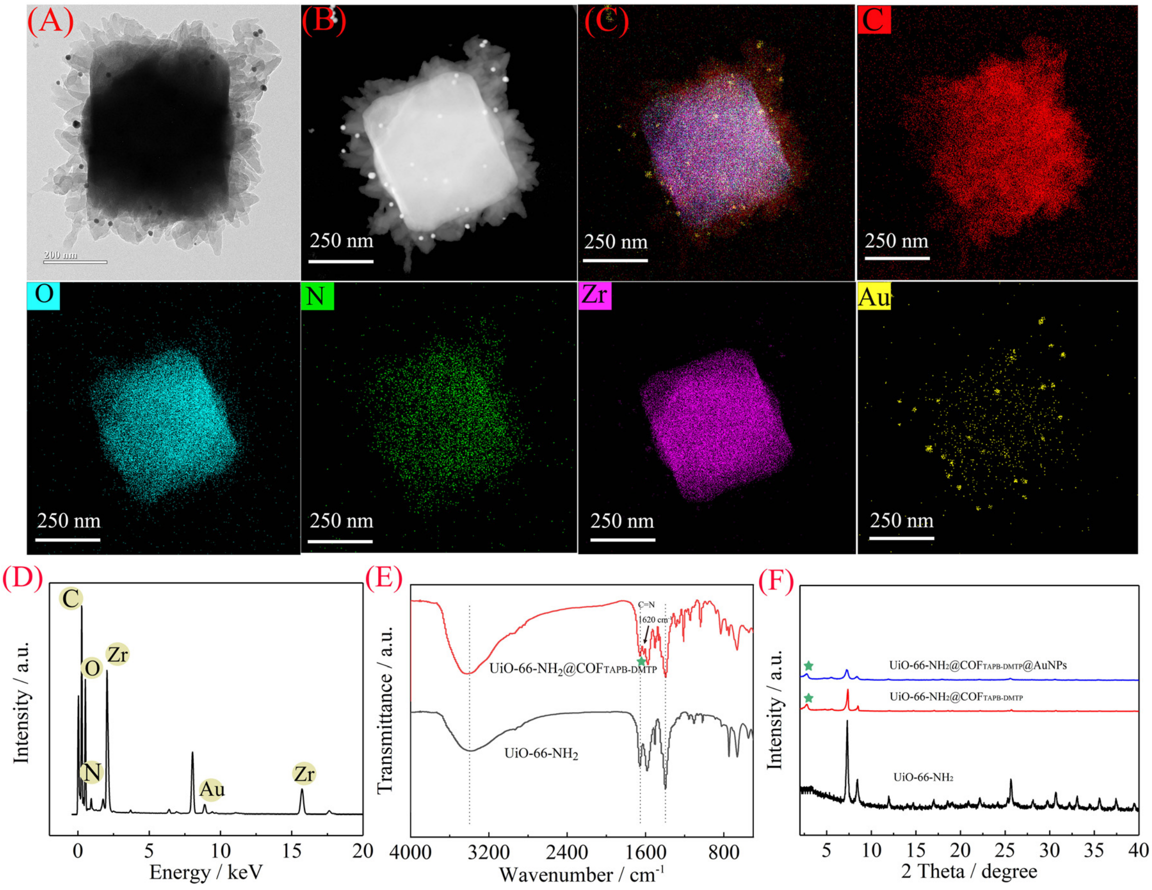

Fig. 2 TEM image of (A) UiO-66-NH_2@$COF_{TAPB-DMTP}$@AuNPs, (B) dark-field in HAADF images of UiO-66-NH_2@$COF_{TAPB-DMTP}$@AuNPs and (C) TEM elemental mapping images. (D) The EDS image of UiO-66-NH_2@$COF_{TAPB-DMTP}$@AuNPs. (E) FT-IR spectra of UiO-66-NH_2 and UiO-66-NH_2@$COF_{TAPB-DMTP}$. (F) XRD results of UiO-66-NH_2, UiO-66-NH_2@$COF_{TAPB-DMTP}$ and UiO-66-NH_2@$COF_{TAPB-DMTP}$@AuNPs.

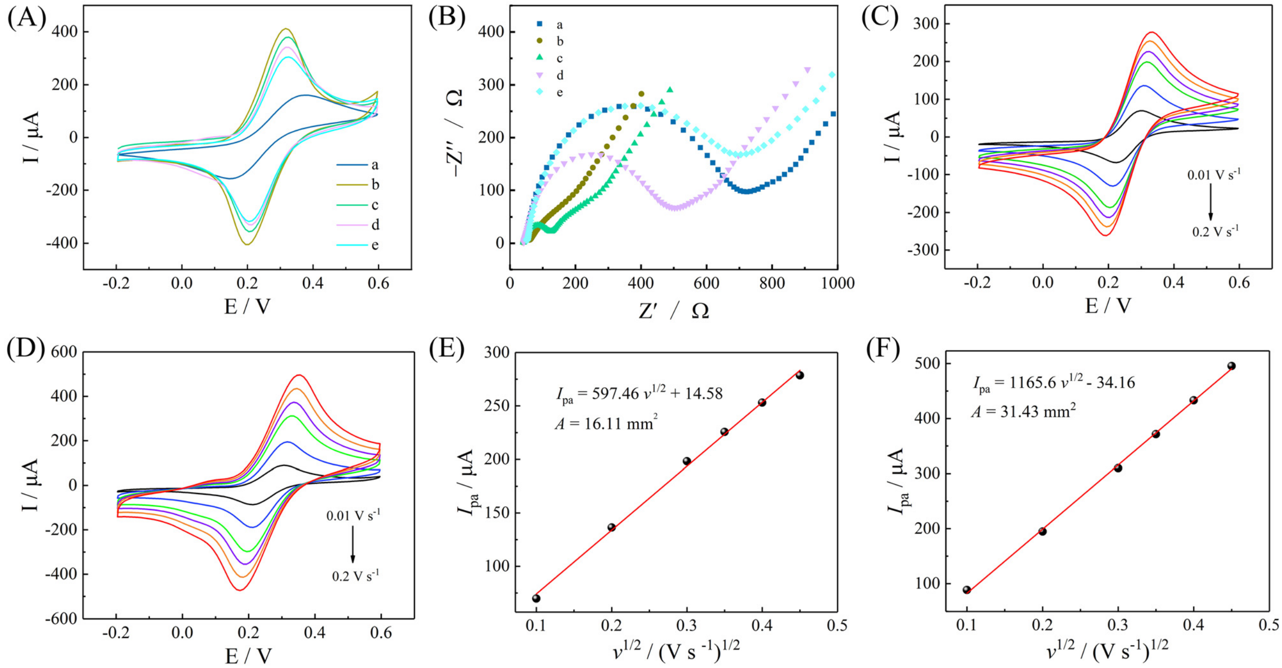

Fig. 3 CV curves (A) and EIS spectra (B) for characterization in 5 mM $K_3[Fe(CN)_6]/K_4[Fe(CN)_6]$ 0.1 M KCl: (a) bare GCE, (b) P-NG-AuNPs/GCE, (c) CP/P-NG-AuNPs/GCE, (d) BSA/CP/P-NG-AuNPs/GCE, and (e) ctDNA/BSA/CP/P-NG-AuNPs/GCE. The dependence of redox peak currents of (C) the bare GCE and (D) the P-NG-AuNPs/GCE at different scan rates (0.01 V s^{-1} to 0.2 V s^{-1}). The calibration plots of oxidation peak current *versus* square root of scan rate for (E) the bare GCE and (F) the P-NG-AuNPs/GCE.

has similar XRD peak intensities and distributions to UiO-66-NH_2@$COF_{TAPB\text{-}DMTP}$, indicating that the introduction of AuNPs does not cause any change in the crystal structure of UiO-66-NH_2@$COF_{TAPB\text{-}DMTP}$.

3.2. Electrochemical characterization of the prepared DNA biosensor

The stepwise construction process at the electrode surface was characterized by cyclic voltammetry (CV) and electrochemical impedance spectroscopy (EIS). As shown in Fig. 3A, the bare GCE exhibited a low current response of 160.8 μA (curve a). After modifying the GCE with P-NG-AuNPs, the electrode showed a significantly increased current of 412.3 μA (curve b). Subsequent immobilization of the CP reduced the CV response to 379.8 μA (curve c), followed by a further decrease to 341.0 μA after blocking non-specific binding sites with BSA (curve d). Finally, ctDNA was immobilized *via* complementary base pairing to the CP, yielding a peak current of 304.6 μA (curve e).

As demonstrated in Fig. 3B, the EIS quantified the electron transfer resistance (R_{ct}) at each step: the bare GCE exhibited a high R_{ct} (703 Ω, curve a). After incubation of the P-NG-AuNPs, their excellent conductivity caused the resistance to dramatically decreased to 67.9 Ω (curve b). The R_{ct} subsequently increased to 122 Ω with CP functionalization (curve c), rose further to 502 Ω after BSA blocking (curve d), and reached 671 Ω upon ctDNA immobilization (curve e). These consistent trends between EIS and CV data confirm the successful construction of the biosensor.

3.3. Investigation of the effective specific surface area of different modified electrodes

The electrochemical performance of the modified electrode is dependent on its effective area. To investigate whether the P-NG-AuNPs composite enhances the effective specific surface area (A, mm^2), cyclic voltammetry (CV) was performed. The bare GCE and P-NG-AuNPs/GCE were tested in a 5 mM $K_3[Fe(CN)_6]/K_4[Fe(CN)_6]$ solution at different scan rates (v, V s^{-1}). The anodic peak currents (I_{pa}, A) of the bare GCE (Fig. 3C and D) and the P-NG-AuNPs/GCE (Fig. 3E and F) exhibited a linear relationship with the square root of the scan rate ($v^{1/2}$). Based on the Randles–Sevcik equation[32] and the slope of the calibration curve, the effective specific surface area (A) of the P-NG-AuNPs/GCE was calculated to be 31.43 mm^2 (calculation details are provided in Section S6, ESI†), significantly exceeding that of the bare GCE (16.11 mm^2). These results demonstrate that the P-NG-AuNPs/GCE can increase the effective area of the electrode and promote the electron transfer on the electrode surface.

3.4. Optimization of experimental parameters

To optimize ctDNA detection conditions, key experimental parameters were systematically adjusted to enhance the performance of the method, with detailed optimization procedures provided in Section S8 (ESI†).

3.5. DPV responses and calibration curve

To systematically evaluate the detection performance of the sensor, the electrochemical response of ctDNA in the concentration gradient from 1 fM to 100 nM was measured by DPV under

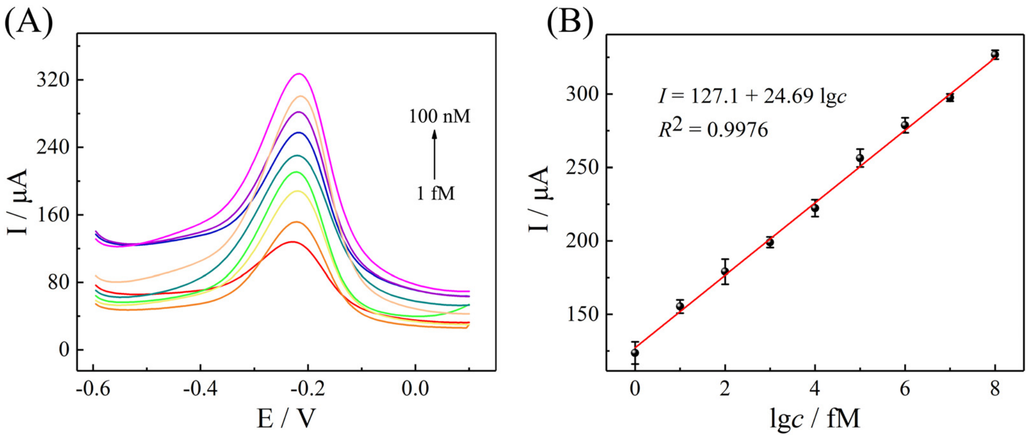

Fig. 4 (A) The DPV response of the biosensor with different concentrations of ctDNA was detected in 0.1 M PB (pH = 7). (B) The calibration plot between the current response and the concentration logarithm. Error bars represent the standard deviation (n = 3).

optimized experimental parameters. The DPV peak current exhibited a concentration-dependent increase with rising ctDNA levels (Fig. 4A), and a strong linear correlation (R^2 = 0.9976) was observed between the current response and the logarithm of ctDNA concentration over the range of 1 fM to 100 nM.

The standard calibration curve was expressed as $I = 24.69\,\lg c + 127.1$ (Fig. 4B), with a calculated limit of detection (LOD) of 0.31 fM (3s/m, where s represents the standard deviation of the blank solution and m is the slope of the calibration curve). Compared with the existing ctDNA detection methods reported in the literature (Table S1 of the ESI†), the developed sensor exhibited superior performance in critical metrics, including the linear detection range and LOD.

3.6. Stability studies, specificity and reproducibility

As shown in Fig. 5A, the current response to 100 pM ctDNA remained stable over five consecutive scan cycles, which

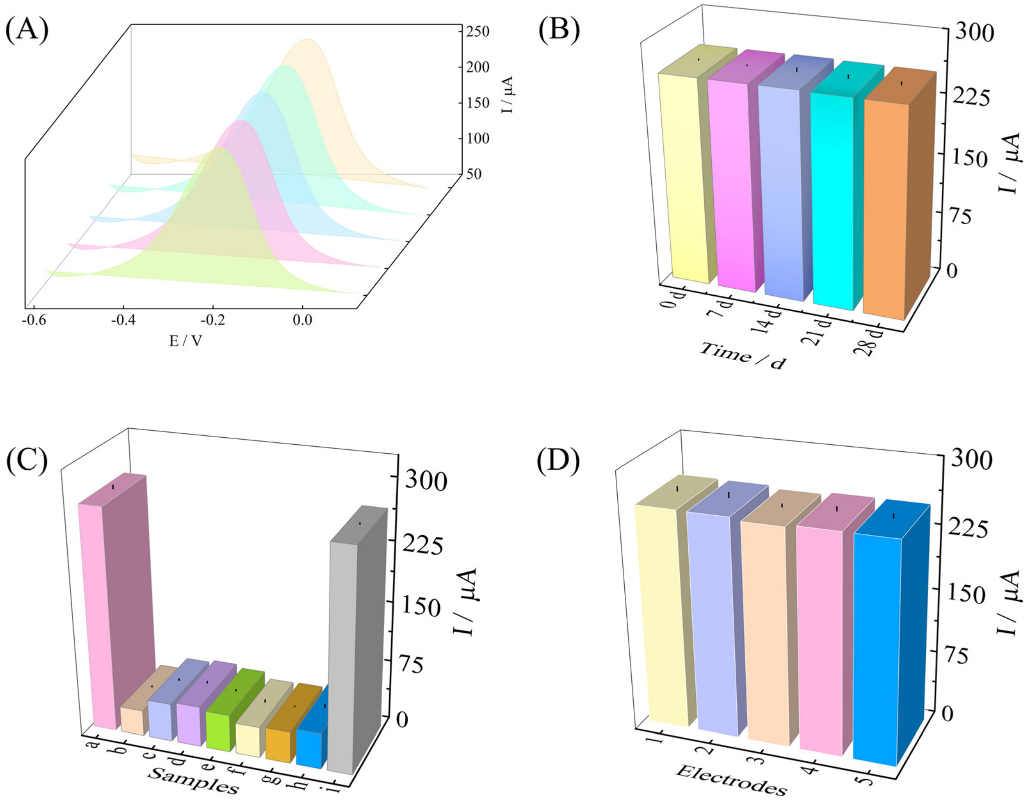

Fig. 5 (A) Short-term stability of the DNA biosensor after 5 continuous scans. (B) Long-term stability of the DNA biosensor for 28 days. (C) Specificity of the DNA biosensor with various interfering substances (a → g: ctDNA, blank, N-DNA, D-DNA, S-DNA, urea, AA, Glu, and mixture). (D) Reproducibility of the DNA biosensor. Error bars represent the standard deviation (n = 3).

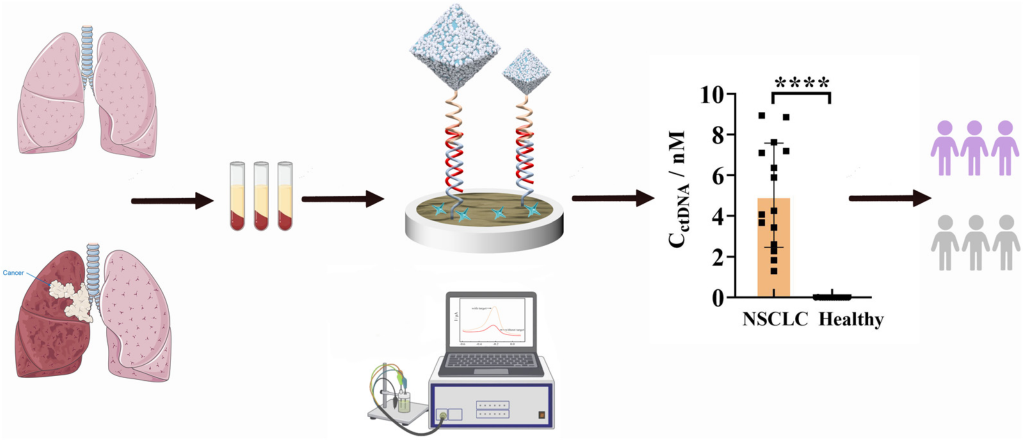

Fig. 6 The method and outcomes of the suggested biosensor for ctDNA detection in NSCLC patients and healthy donors.

initially demonstrated the stability of the biosensor to a certain extent.

The current response of the prepared biosensor remained at 99.61% of the initial current after 28 days of storage at 4 °C (Fig. 5B). This result demonstrates that the electrochemical biosensor has excellent stability and can maintain stable performance over a long period of time and under specific conditions, which provides strong support for its reliability in practical applications.

The results of selectivity validation experiments showed that the DNA biosensor exhibited excellent analytical performance in complex biological matrices (Fig. 5C). In the experimental design, we used a stepwise concentration gradient strategy: the detection concentration of non-target DNA molecules (N-DNA, D-DNA, and S-DNA) was elevated to 100-fold (100 nM) that of the target ctDNA (1 nM). It is noteworthy that even in the presence of mismatched DNA interference from single base differences, the biosensor can effectively discriminate between the target ctDNA and the interfering substance. The current response of the ctDNA shows significant differences compared to the blank control and interference groups. The effects of common biological interferences (dopamine, ascorbic acid, and glucose, urea) on the detection system were also investigated, and the experimental data showed that ctDNA-specific detection signals revealed little variation in the presence of high interferences. The above results indicated that the sensor platform has accurate molecular recognition capability and anti-interference capability.

DPV responses of five modified electrodes incubated with 100 pM ctDNA were measured sequentially under optimal conditions (Fig. 5D). The experimental results showed that the five modified electrodes produced similar DPV responses with a relative standard deviation (RSD) of 0.60%. This indicates that the proposed sensor has satisfactory reproducibility.

3.7. Detection in real samples

The ctDNA was added to healthy human serum to analyze the potential of this electrochemical biosensor for clinical diagnostic applications. The blood samples were first pre-treated and then centrifuged at 3000 rpm for 10 min to isolate the serum. The serum was diluted 50-fold in 0.1 M phosphate buffer (PB, pH 7.0). The results obtained using the prepared DNA biosensor for a concentration gradient of ctDNA (Table S2, ESI†) showed recoveries ranging from 85.17% to 103.2%, with an RSD of 6.63–9.45%. This indicates that the method has acceptable analytical reliability.

3.8. Potential clinical application analysis

In order to further evaluate the usefulness of the DNA biosensor, as shown in Fig. 6, the serum ctDNA concentration of 15 patients with non-small cell lung cancer (NSCLC) was compared with those from 15 healthy control subjects. The patient group exhibited significantly higher ctDNA concentrations compared to the healthy group ($p < 0.05$). The experimental data confirm that this DNA biosensor platform not only achieves efficient detection of ctDNA from complex biological matrices but also accurately distinguishes pathological samples from normal samples, demonstrating its clinical applicability in tumor marker detection.

4. Conclusions

In this study, we successfully applied the MOF@COF material to a DNA biosensor by loading more signaling molecule MB through its core–shell structure, which improved the sensitivity of the biosensor. Experimental results demonstrated that the biosensor has excellent selectivity, stability, and reproducibility, effectively differentiating ctDNA levels between NSCLC patients and healthy individuals. Although the preparation process of this DNA biosensor still has some complexity, the successful application of its MOF@COF material provides a significant technical reference in the field of ctDNA detection. Future work will focus on streamlining biosensor assembly without compromising analytical performance.

Author contributions

Lin Fu: conceptualization, methodology, formal analysis, writing – original draft, funding acquisition, and visualization.

Xiaolin Yu: funding acquisition and visualization. Yan Zhang, Huiling Chen and Junxin Li: resources and project administration. Min Shi, Yanyu Li and Gongli Hu: validation and investigation. Peng Tang: writing – review and editing and visualization. Zhongshu Wang and Yi Xiao: methodology, resources, writing – review and editing, and project administration.

Conflicts of interest

The authors declare that they have no known competing financial interests or personal relationships that could have appeared to influence the work reported in this study.

Ethical approval

All experiments were performed by the guidelines ''Declaration of Helsinki'' and were approved by the Ethics Committee of Zigong Fourth People's Hospital (approval no. EC-2025-105).

Data availability

The data that support the findings of this study are available on request from the corresponding author, Yi Xiao, upon reasonable request.

Acknowledgements

This work is supported by the China Population Welfare Foundation Healthy China-Action-Medical Research Qi Xing Program (SLB-2-20250507-161) and the Sichuan Science and Technology Program (2022NSFSC0810).

References

1 F. Bray, M. Laversanne, H. Sung, J. Ferlay, R. L. Siegel, I. Soerjomataram and A. Jemal, *CA: Cancer J. Clin.*, 2024, **74**, 229–263.

2 R. Rosell, T. G. Bivona and N. Karachaliou, *Lancet*, 2013, **382**, 720–731.

3 A. A. Thai, B. J. Solomon, L. V. Sequist, J. F. Gainor and R. S. Heist, *Lancet*, 2021, **398**, 535–554.

4 Y. Zhou, L. Tao, J. Qiu, J. Xu, X. Yang, Y. Zhang, X. Tian, X. Guan, X. Cen and Y. Zhao, *Signal Transduction Targeted Ther.*, 2024, **9**, 132.

5 D. Zhong, Z. Wang, Z. Ye, Y. Wang and X. Cai, *Molecular Cancer*, 2024, **23**, 67.

6 K. Chen, F. Yang, H. Shen, C. Wang, X. Li, O. Chervova, S. Wu, F. Qiu, D. Peng and X. Zhu, *Cancer Cell*, 2023, **41**, 1749–1762.

7 L. Peng, Y. Bin, P. Ding, L. Chen, H. Zeng, Z. Xu, L. Ji, X. Gao, P. Liu and Y. Wang, *Cancer Commun.*, 2023, **43**, 625.

8 C. Abbosh, N. J. Birkbak, G. A. Wilson, M. Jamal-Hanjani, T. Constantin, R. Salari, J. Le Quesne, D. A. Moore, S. Veeriah and R. Rosenthal, *Nature*, 2017, **545**, 446–451.

9 C. Abbosh, D. Hodgson, G. J. Doherty, D. Gale, J. R. M. Black, L. Horn, J. S. Reis-Filho and C. Swanton, *Trends Cancer*, 2024, **10**, 643–654.

10 N. Balasan, F. Kharrat, G. Di Lorenzo, E. Athanasakis, A. M. Bianco, A. Conti, M. T. Di Stazio, G. Butera, S. Cicogna, A. Mangogna, F. Romano, G. Ricci and A. P. d'Adamo, *Int. J. Mol. Sci.*, 2024, **25**, 11997.

11 L. Shen, P. Wang and Y. Ke, *Adv. Healthcare Mater.*, 2021, **10**, 2002205.

12 S. Barrias, J. Ibáñez, J. R. Fernandes and P. Martins-Lopes, *Trends Food Sci. Technol.*, 2024, **145**, 104350.

13 J. Wang, X. Cui, L. Liang, J. Li, B. Pang and J. Li, *Talanta*, 2024, **275**, 126072.

14 Y. Hua, J. Ma, D. Li and R. Wang, *Biosensors*, 2022, **12**, 183.

15 J. Park, Y. Choi, S. Jeon, S. Kee, E. Na and M. Shin, *Clin. Chem.*, 2024, **70**, hvae106.551.

16 L. Guo, Z. Mu, B. Yan, J. Wang, J. Zhou and L. Bai, *Sens. Actuators, B*, 2022, **350**, 130874.

17 L. Duan, H. Jin, Y. Wen, M. Wei, R. Guo, Z. Suo and K. Niranjan, *Sens. Actuators, B*, 2025, **438**, 137780.

18 D. He, N. Dong, Y. Li, D. Liu and T. You, *Anal. Chim. Acta*, 2025, **1342**, 343661.

19 Y. Zhu, L. Chen, J. Pan, S. Jiang, J. Wang, G. Zhang and K. Zhang, *Prog. Mater. Sci.*, 2025, **148**, 101373.

20 M. Chafiq, A. Chaouiki and Y. G. Ko, *Energy Storage Mater.*, 2023, **63**, 103014.

21 D. Sun, S. Jang, S.-J. Yim, L. Ye and D.-P. Kim, *Adv. Funct. Mater.*, 2018, **28**, 1707110.

22 L. Garzón-Tovar, J. Pérez-Carvajal, A. Yazdi, J. Hernández-Muñoz, P. Tarazona, I. Imaz, F. Zamora and D. Maspoch, *Angew. Chem.*, 2019, **58**, 9512–9516.

23 Z. Wu, W. Li, L. Hou, Q. Wei, H. Yang, Y. Jiang and D. Tang, *Sep. Purif. Technol.*, 2023, **311**, 123322.

24 H.-Y. Zhang, Y. Yang, C.-C. Li, H.-L. Tang, F.-M. Zhang, G.-L. Zhang and H. Yan, *J. Mater. Chem. A*, 2021, **9**, 16743–16750.

25 H. Zhang, Y. Cao, W. Li, S. Zhang, S. Song, Y. Wang and H. Zhang, *Chem. Eng. J.*, 2024, **493**, 152675.

26 X. Yu, J. Li, M. Du, X. Song, H. Huang and L. Nie, *Cell Rep. Phys. Sci.*, 2023, **4**, 101657.

27 J. Li, B. Zhang, P. Liu, Y. Chen, Y. Liu, J. Li and L. Li, *J. Colloid Interface Sci.*, 2024, **669**, 258–264.

28 Z. Ye, W. Liao, Z. Deng, L. Wang, B. Wen, D. Zhang, H. Wang, W. Xie and H. Peng, *TrAC, Trends Anal. Chem.*, 2024, **175**, 117724.

29 H.-W. Zhang, Q.-Q. Zhu, R. Yuan and H. He, *Sens. Actuators, B*, 2021, **329**, 129144.

30 X. Jiang, Z. Mu, J. Wang, J. Zhou and L. Bai, *Food Chem.*, 2024, **436**, 137704.

31 Z. Yu, D. Wang, T. Zheng, A. Zavabeti, Y. Wang, C. Wu, J. Yang, Y. Guo, P. A. Webley and G. K. Li, *J. Mater. Chem. A*, 2025, **13**, 8368–8374.

32 W. Yang, T. Huang, M. Zhao, F. Luo, W. Weng, Q. Wei, Z. Lin and G. Chen, *Talanta*, 2017, **164**, 1–6.